A Compact Ultralinear Compliant Torsion-Reinforced Sarrus Mechanism

Van Velden, Joran L.; Herder, Just L.

DOI
10.1115/1.4069977

Publication date
2026

Document Version
Final published version

Published in
Journal of Mechanisms and Robotics

ASME Journal of Mechanisms and Robotics
Online journal at:
https://asmedigitalcollection.asme.org/mechanismsrobotics

A Compact Ultralinear Compliant Torsion-Reinforced Sarrus Mechanism

Joran L. van Velden[1]
Department of Mechanical Development,
VDL ETG Technology & Dev. B.V.,
De Schakel 22, 5651GH, Eindhoven,
Noord-Brabant, The Netherlands
e-mail: Joran.van.velden@vdletg.com

Just L. Herder
Faculty of Mechanical Engineering,
Delft University of Technology,
Mekelweg 2, 2628CD, Delft,
Zuid-Holland, The Netherlands
e-mail: J.L.Herder@tudelft.nl

In this study, a promising design for a compact compliant torsion-reinforced Sarrus mechanism (CORS) capable of achieving ultralinear motion is presented. The CORS prototype, made entirely of aluminum, is produced monolithically using electric discharge machining (EDM). The design incorporates four torsion-reinforced folded leaf springs that together function as a flexural mechanism. This design effectively reduces parasitic motion while improving support stiffness. To meet the specified requirements, a design optimization process is undertaken, carefully considering constraints, to attain an optimal CORS configuration. Integration of the CORS with a voice coil actuator and confocal chromatic sensors is carried out to detect parasitic motion. Experimental validation demonstrates that the CORS outperforms existing designs in terms of build volume, manufacturability, and scalability, and has parasitic translations of around 10 nm and parasitic rotations of around 5 μrad over the critical region of the range of motion.
[DOI: 10.1115/1.4069977]

Keywords: ultralinear stage, compliant mechanism, Sarrus mechanism, parasitic motion, monolithic

1 Introduction

Ultraprecision mechanisms with one, two, or three degrees-of-freedom (DoFs) are the foundation for applications such as semiconductor fabrication [1,2], scanning systems [3,4], medical imaging [5], and nanodevice fabrication [6,7]. These industries demand devices that allow for precision motion guidance with a resolution and accuracy in the order of micrometers or even nanometers. For example, in the semiconductor industry, the trend is to make microchips smaller and faster, with feature resolutions of up to 10 nm [8].

In photolithography, which is a core process in semiconductor manufacturing, precise motion mechanisms are critical during the alignment and exposure stages. In the optical and photonic industry, precise motion mechanisms are crucial to enable precise motion to scan surfaces or adjust focal planes and optical paths, for instance. All of these applications have a common principle: Varying the gap between two bodies. In this study, the application of varying the gap between a mask or lens, i.e., optical elements, and a substrate is used. This study explores the potential for moving the optical element to enhance the coupling dynamics. Compared to the heavier substrate stage, the lower mass of the optical element allows for faster and more precise motion with reduced vibration. However, implementing a moving optical element involves a complex building volume. Conventionally, the optical element is positioned close to both the metrology and the substrate, resulting in an intermediary volume with limited height in the direction of motion. Furthermore, this volume is predominantly maintained under vacuum conditions, imposing additional constraints on mechanical design and integration. Ultraprecision stages typically integrate a compliant mechanism (CM) to facilitate motion guidance, making them well-suited for applications requiring ultralinear vertical movement.

CMs use elastic deformation of flexible components to enable a desired motion due to a force or input motion. There are multiple advantages of CM for precise positioning. Due to their elastic nature, these mechanisms have no friction, no backlash, and are linearly predictable for small motions [9]. Furthermore, CMs benefit from the fact that there are no overlapping pieces which can allow single-piece production [10]. This bears potential for significantly lower costs as a result of less assembly and manufacturing time. However, CMs are more challenging to design due to their inherent coupling between kinetics and kinematics [11].

Focusing on straight-line mechanisms that are suitable as an ultraprecision stage, the available literature is scarce. Nevertheless, several researchers have developed different types of ultralinear stages using CM, which can be summarized on the basis of three categories: spatial mechanisms, planar mechanisms, and out-of-plane planar mechanisms.

Spatial geometries include geometries in the 3D coordinate system. The flexible elements are not in the same plane as the motion. Koster has developed ARCADE [12]. This stage has a stroke of 5 mm and deviates along the X and Y axes by at most 15 nm and rotates around these axes with less than 5 μrad. Cosandier created a translational stage for the Watt balance [13]. This mechanism deviates up to 180 nm and 40 nm along the X and Y axes, respectively, while rotations did exceed 5.3 μrad around the Y axis and 3 μrad around the X axis. Furthermore, Cosandier designed an assembled Sarrus guide. The parasitic motions are promising along the stroke of 40 mm. Translational deviations along the X and Y axes are within 200 nm and 500 nm, respectively, while the rotations in the X and Y axes are around 275 μrad and 220 μrad, respectively.

Next to spatial geometries are planar geometries where the flexible elements are in-plane with the motion. Duarte et al. built a rectilinear motion machine based on flexural principles [14]. Their focus was on the tilt angle that is reported to deviate at most 1.8 μrad. Smith et al. designed a monolithic spring mechanism [15]. Their design allowed a displacement of 0.05 mm. The mechanism deviates by 5 nm and 4000 nm along the X and Y axes, respectively. Furthermore, they measured a pitch error of 250 nrad. Nicolas et al. designed a mechanism enabling a stroke of 24 mm with a maximal

[1]Corresponding author.

Contributed by the Mechanisms and Robotics Committee of ASME for publication in the Journal of Mechanisms and Robotics. Manuscript received August 16, 2025; final manuscript received September 22, 2025; published online October 17, 2025. Assoc. Editor: Nilanjan Chakraborty.

parasitic motion of 1 μm in the translational directions and a parasitic rotation below 100 μrad [16]. Becker et al. claimed a smooth translation within one hundredth of a nanometer, and tilt below 1 nrad over the full range of motion [17]. In order to reduce the parasitic motions, they added additional torques proportional to the displacement using magnets. Jones designed a mechanism for a 10 mm stroke, which deviates by 2000 nm and 500 nm in the *X* and *Y* directions [18]. The measured parasitic rotations were 10 μrad, 63 μrad, and 136 μrad for yaw, pitch, and roll, respectively. Alemanni et al. have designed a mechanism capable of a parasitic rotation of 3.6 μrad around the *X*-axis along a stroke of 0.13 mm [19]. Tissot-Daguette et al. proposed a new design with a maximum parasitic translation of 65.6 nm and was observed in the finite element analysis (FEA) along a stroke of 8 mm [20]. The occurring parasitic roll motion was 13.6 μrad.

Out-of-plane planar geometries have an in-plane geometry but an out-of-plane motion, which enables compact designs, and they are referred to as orthoplanar springs [21]. They are often used as motion guides in ultraprecision stages. Chen et al. designed and optimized an out-of-plane 1-DoF mechanism [22]. They have maximized the ratio of the radial stiffness to the out-of-plane drive stiffness. Over a range of 0.14 mm, they observed 2000 nm of deviation along the *X* and *Y* axes. Around the *X* and *Y* axes, a rotation of 26 μrad was observed. Orthoplanar springs typically allow only small displacements. Furthermore, they lack significant support stiffness, making them sensitive to undesired rotations and translations.

Planar geometries are easier to manufacture, resulting in lower cost and improved manufacturing tolerances. However, their motion is in the same plane as the flexure, which often results in a large build volume in the direction of motion. Spatial CMs, such as the Sarrus mechanism, are often large in size and more difficult to manufacture. However, the Sarrus mechanism is a spatial mechanism that potentially has a smaller building volume in the direction of motion. Thus, there is a need for an easy to manufacture compliant Sarrus mechanism with a small build volume in the direction of motion and reduced parasitic motion.

In this study, a promising design of a compact ultralinear compliant torsion-reinforced Sarrus mechanism (CORS), capable of ultralinear motion, is presented. Due to its compactness, a less obstructive build volume is required as compared to existing stages. A mathematical model is developed, and stiffness values are calculated. A finite element model (FEM) is developed in the Simcenter HEEDS program suite to optimize the CORS. An experimental evaluation to verify the FEM model was conducted on an aluminum 5083-O prototype made by means of electric discharge machining (EDM).

This article is organized as follows. Section 2 describes the methods used in this study, outlining the design criteria, conceptual design, dimensional design, and design optimization. In Sec. 3, the experimental validation is presented, providing detailed descriptions of the test setup, experiments conducted, and the corresponding results. Following this, Sec. 4 offers a discussion on the findings, contextualizing them and exploring their implications. Finally, Sec. 5 concludes this article by summarizing the key findings, reflecting on the significance of the research, and suggesting recommendations for future research.

2 Methods

2.1 Design Criteria. In the design of the CORS, design criteria were considered based on the field of application. The reference frame used has *X* and *Y* situated in the horizontal plane and *Z* pointing upwards.

The first criterion states that the CORS must enable a platform to perform a 5 mm translation along the *Z*-axis, of which the last 140 μm are critical for the application at hand.

The second criterion states that the CORS must effectively mitigate horizontal parasitic motions of the platform. These motions encompass translations Tx and Ty along both the *X* and *Y* axes, respectively, as well as rotations around the *X*-axis (Rx, tip), *Y*-axis (Ry, tilt), and *Z*-axis (Rz, twist). The cumulative parasitic motion, or total error budget, denoted as *e*, remains within 5 nm over the critical 140 μm region of the 5 mm stroke, which is the critical region of the range of motion for the application. Among the contributing factors, twist-induced deformation is expected to dominate the horizontal parasitic motion. For an optical element with a characteristic length of 150 mm, a rotational deviation of 50 nrad results in an estimated horizontal parasitic displacement of approximately 5 nm, assuming the rotational axis in the center.

The third criterion involves the stiffness of the CORS. The first eigenfrequency must be below 20 Hz to limit the actuation force since high forces can lead to high unwanted internal stresses. Furthermore, the second (and subsequent) eigenfrequency must be maximized to improve the controllability, robustness, and dynamic performance.

The last criterion describes the available volume: the CORS has to fit in a rectangular space of $300 \times 300 \times 45$ mm. An overview of the design criteria is given in Table 1.

2.2 Conceptual Design. The CORS presented here is based on a conventional Sarrus linkage [23]. The Sarrus mechanism is a well-known rigid link mechanism, comprising four links organized into two perpendicular legs, and characterized by its utilization of two parallel horizontal plates, the base and the platform, arranged one above the other (Fig. 1). Each leg features a pair of hinged links, connecting the base to the platform, facilitating vertical motion of the platform relative to the base. The hinges enforce constraints, ensuring that the links of each leg remain in their respective planes. Together they allow vertical translation of the platform. Mobility analysis indicates zero DoFs for the two-sided Sarrus linkage. However, closer analysis yields that the platform has one DoF (Tz) and one overconstraint. More legs can be added, increasing the number of overconstraints.

The rigid link Sarrus mechanism can be transformed into a CM, leading to the CORS design as follows. The links in the legs are replaced by flexures, two leaf springs under an angle in series for each leg. Such a set of two leaf springs is also known as a folded

Table 1 Overview of the design criteria

Criterion	Value
DoFs	1 (*Z*-translation)
Range of motion	5 mm
Cumulative error	5 nm
f_0	<20 Hz
Volume	$300 \times 300 \times 45$ mm

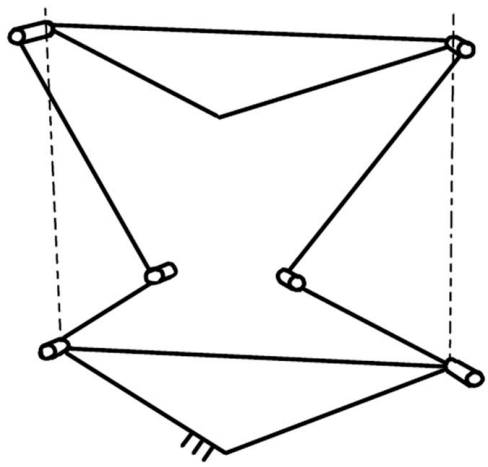

Fig. 1 Schematic of the Sarrus linkage

leaf spring [24], where the two leaf springs are typically oriented 90 deg relative to each other. Other angles are possible as long as the leaf springs are not aligned. Each leg is thus a folded leaf spring. In general, the parameters that define the mechanism are the number of flexures, the inter-flexure angle, and relative orientation of the legs. The characteristics defining a single leaf spring are length, width, and thickness.

A folded leaf spring only constrains one DoF, namely, the translation along its folding axis (*X*-axis in Fig. 2) [24]. Since it is a spatial mechanism, the torsional compliance of a single leaf spring needs to be taken into account besides the compliance along the *X*, *Y*, and *Z*-axis. The torsional stiffness is

$$K_t = \frac{GJ}{L} \tag{1}$$

where $J = \frac{1}{3}dt^3$ is the torsion constant and G is the shear modulus. Increasing this torsional stiffness results in constraining one more DoF. The bending stiffness around the folding axis, *X*, is

$$K_{rx} = \frac{EI_{rx}}{L} \tag{2}$$

where the area moment of inertia around the folding axis is $I_{rx} = \frac{1}{12}dt^3$.

Furthermore, the in-plane bending stiffness has to constrain an additional DoF. The in-plane bending stiffness of the leaf spring is

$$K_{ipb} = \frac{EI_{ipb}}{L} \tag{3}$$

where $I_{ipb} = \frac{1}{12}td^3$. This stiffness has a higher order of magnitude relative to K_t and K_{rx}. Therefore, it is assumed to be constrained.

Increasing torsional stiffness is achieved by incorporating torsion-reinforcement structures onto the leaf springs in the form of triangles that each are composed of a section of the original leaf spring plus two additional ones in a triangle configuration. These structures, previously introduced by Rommers et al., effectively suppress torsion of the original flexure and are used to create a flexure joint with high stiffness in its support directions [25]. A torsion-reinforced folded leaf spring will result in constraining three-DoF. The reinforcement structures behave like flexures with distributed compliance resulting in a smooth strain distribution. As a result, two new parameters are introduced: n and γ, where n is the number of reinforcements (further referred to as teeth) and γ is the angle of the teeth leaf springs relative to the original spring.

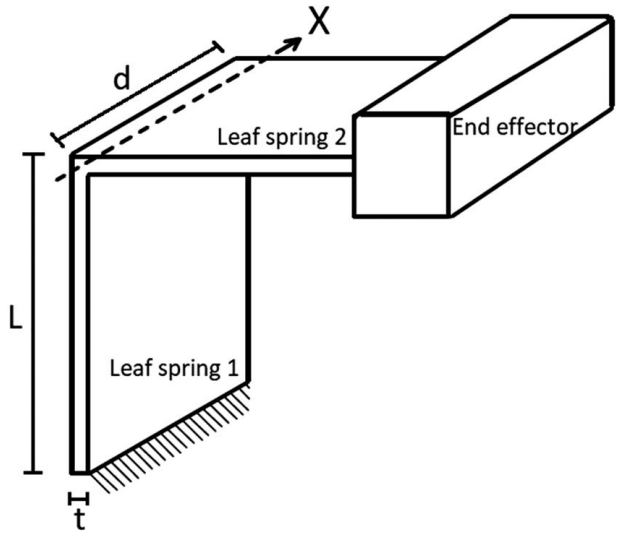

Fig. 2 Illustration of a single folded leaf spring and end effector

Using two torsion-reinforced folded leaf springs, in this case oriented at 90 deg relative to each other, leads to a concept of a compliant Sarrus mechanism. The combination of two reinforced folded leaf springs, a total of six constraints, is present. Similar to the rigid link Sarrus, the specific configuration results in one DoF and one overconstraint. The DoF is a translational motion perpendicular to both folding axes.

As a next step, it was decided to add two more reinforced folded flexures, arriving at a total of four legs, as in Fig. 3. This choice was made because of the manufacturability and symmetry and to create a rectangular form that is more generally applicable as compared to three symmetric flexures resulting in a triangular platform. Furthermore, it also results in a centered center of stiffness which is proven to be beneficial to minimize parasitic motions [26]. The width of the flexures influences the reliability of the EDM manufacturing process. The effective spark height must be minimized to reduce manufacturing errors. The configuration with four folded leaf springs leads to a minimized spark height while maintaining high support stiffness or even increasing the stiffness in nonmotion directions. Due to a centered center of stiffness, it is easier to actuate in the center of stiffness because it is precisely known, which is another strategy to prevent parasitic motion according to Ref. [26]. This configuration (Fig. 3) results in a seven times overconstrained system, which can result in unwanted stresses and nondeterministic behavior [27]. However, adding overconstraints has been proven beneficial in some cases and has less influence in a monolithic structure [28]. The overconstraints can help compensate for manufacturing imperfections by elastic averaging of small misalignments or asymmetries [29].

Each parameter within the CORS must be carefully defined based on trade-offs. For example, the thickness and width of flexures should ideally be maximized to enhance constraint levels. However, this maximization is limited by the need to maintain a low eigenfrequency, i.e., low stiffness in the range of motion [30]. Additionally, minimizing the inter-flexure angle is advantageous for reducing the stiffness in the direction of motion and increasing lateral stiffness, while an angle of zero theoretically leads to a mechanism reliant on leaf spring compression. However, this angle is limited due to manufacturability.

Another parameter to consider is the number of reinforcement teeth, which involves a trade-off between building volume and torsional stiffness. Increasing the number of teeth reduces building volume, assuming a constant γ, while improving torsional stiffness. However, this also leads to increased stiffness in the direction of motion, potentially requiring multiple formed triangles to bend in a chain-like manner. Achieving an optimal balance among these parameters is essential for designing the CORS that meets performance requirements while minimizing constraints.

2.3 Dimensional Design and Modeling

2.3.1 Design Parameters and Performance Metrics. The flexures of the mechanism, folded leaf springs and teeth, can be defined by the parameters illustrated in Fig. 4. The thickness of the top and bottom flexures are defined as t_t and t_b, respectively. Furthermore, the width of the platform and the flexure are defined as b and d, respectively. The number of teeth is addressed with n_t and n_b.

2.3.2 Stiffness Analysis. The direct method is used for a numerical 3D beam finite element analysis considering bending, small displacements, and no cross-axis couplings.

$$\mathbf{f} = \mathbf{Kd} \tag{4}$$

where $\mathbf{f}$ is the nodal load vector with three forces along and three moments around the *XYZ*-axes for each node, $\mathbf{K}$ is the system matrix, and $\mathbf{d}$ is the nodal displacement vector with three translations along and three rotations around the *XYZ*-axes for each node, all in the local coordinate system.

The stiffness matrix of local elements has to be transformed into a global coordinate system. The transformation is performed by the

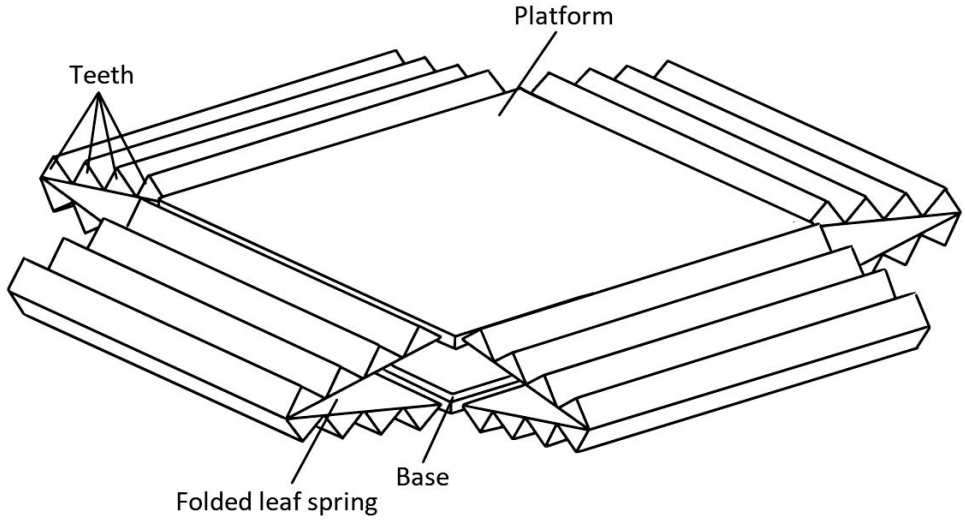

Fig. 3 Illustration of the conceptual design. ***Note that the triangular shapes, labeled "teeth" in the figure, are created by flexure beams creating a hollow triangular structure for each of the teeth.***

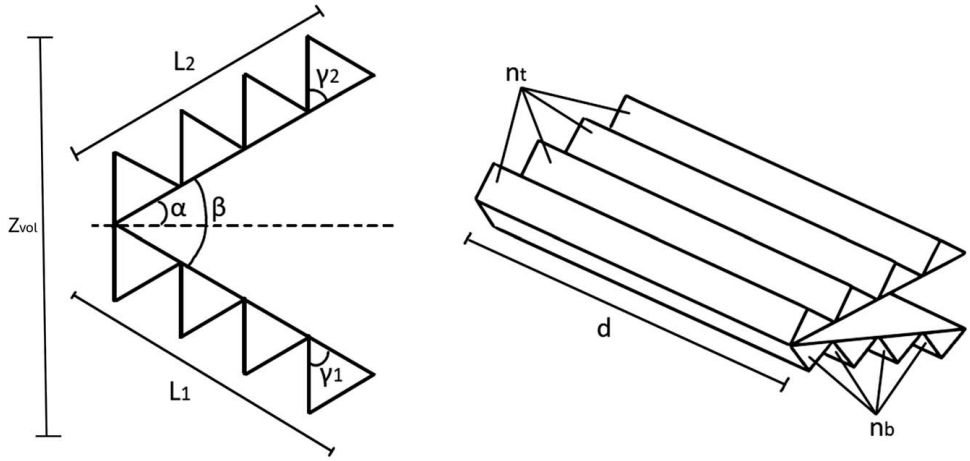

Fig. 4 Illustration of flexure parameters

transformation matrix, **T**, and can be expressed as

$$\mathbf{K}_{\text{global}} = T^T K_{\text{local}} T \tag{5}$$

Once all local element stiffness matrices are computed, the system matrix, **K**, can be assembled. The assembling is done by adding up the virtual work belonging to each of the elements, resulting in the mathematical equivalent of putting the mechanism together:

$$\mathbf{K} = \sum K_{\text{global},1} + \cdots + K_{\text{global},n} \tag{6}$$

The material used for EDM fabrication of the prototype is aluminum, Al 5083-O. The values of α, β, $\gamma_1 = \gamma_2$, $L_1 = L_2$, $t_1 = t_2$, $n_t = n_b$, and $b = d$ of the flexures are 5 deg, 10 deg, 75 mm, 0.6 mm, 1, and 80 mm. The numerically determined value of f_0 is 30 Hz and f_1 is 222.4 Hz, assuming a mass of 700 g.

2.3.3 Optimization in Simcenter HEEDS. To find the optimal design of the CORS, Simcenter Heeds of Siemens (HEEDS) is used. HEEDS can help to gain insight into the design space and find an optimal design according to design criteria and constraints. It is integrated with Siemens NX for parametric sketching and Simcenter for finite element meshing and simulation. HEEDS contains a search strategy called SHERPA, a hybrid, adaptive search strategy that dynamically allocates computational effort between multiple optimization methods, suppressing less effective strategies over time [31].

The iterative workflow involves generating a geometry based on design parameters, meshing, simulating, postprocessing the results, and generating new design parameters based on the results and SHERPA. Each design is evaluated based on a performance function that reflects both objective values and constraint satisfaction. An optimal design is considered achieved when no performance improvement is observed over 200 successive iterations. Additionally, HEEDS provides sensitivity insights, quantifying the influence of individual parameters on performance metrics, thereby enhancing the understanding of the design landscape.

Design Parameters. To ensure flexural symmetry, design parameters are dependent on each other:

$$2\alpha = \beta$$
$$L_1 = L_2 = L$$
$$t_1 = t_2 = t$$
$$\gamma_1 = \gamma_2 = \gamma$$
$$n_t = n_b = n$$

Resulting in the design vector:

$$\mathbf{x} = \begin{bmatrix} \alpha & L & t & \gamma & d & b & n \end{bmatrix}$$

The bounds of **x** are given in Table 2. The bounds are dependent on the specified volume claim and considerations of manufacturability. The lower boundaries for the thickness, t, and the inter-flexure angle, represented by 2α, are related to the limitations of EDM, as informed by the manufacturer's knowledge and assurance. Furthermore, the selection of aluminum 5083-O as the material of choice accelerates the EDM process by a factor of three in comparison to stainless steel or titanium, resulting in reduced costs. Furthermore, the 5083 alloy is cast, resulting in low to zero internal stresses inside the initial workpiece. Minimal internal stress is preferred to avoid geometrical imperfections when the thin flexures are released from the initial workpiece.

Mesh. The mesh should be converged for every design HEEDS generates. Therefore, the mesh should be controlled to ensure a converged robust mesh. In this case, the 2D mesh is used to create an easier controllable surface compared to a 3D solid. The commonly used requirement to use shell elements is that the length characteristic must be significantly larger than another parameter: $L \gg t$, in this case. The benefit of using shell elements is the reduction of computation time relative to solid elements, while maintaining accuracy. An additional benefit for HEEDS is that this allows to run the sensitivity analysis to obtain insight into the design space.

Simulation in Simcenter 3D. The optimization criteria are computed using the simulation software within Simcenter, NASTRAN. One end of the flexures is constrained in all DoFs using a user-defined boundary condition. The enforced displacement acts in the center of the platform. Two solutions contribute to computing the optimization criteria: a modal analysis (SOL 103) and a multistep nonlinear analysis (SOL 401). The outputs are the parasitic translations in the center of the platform, and the first and second eigenmodes of the CORS.

Optimization Problem. The optimization problem can be formulated as follows. The goal is to maximize the difference between the first eigenmode, vertical translation of the platform, and the second parasitic eigenmode. This should be obtained while maintaining stiffness, error, mechanical stress, volume, and manufacturability constraints. Most algorithms benefit from a minimization problem, therefore, it is rewritten into a negative null form:

Minimize

$$\frac{f_0}{f_1}$$

Subject to

$$f_0 - 20 \leq 0$$
$$e - 5 \times 10^{-9} \leq 0$$
$$\sigma_y - 150 \times 10^{6} \leq 0$$
$$Z_{\text{vol}} - 45 \times 10^{-3} \leq 0$$

and

$$\underline{\mathbf{x}} \leq \mathbf{x} \leq \bar{\mathbf{x}}$$

Table 2 Design parameters, their bounds, and optimized values

Variable	Lower bound	Upper bound	Optimized value
$\alpha = \beta$	5	90	5
L	10	150	75
t	0.6	1	0.6
γ	5	89	27
d	10	250	80
b	152	250	152
n	0	6	1

Optimization Results. The resulting optimal design can be seen in Fig. 5, the prototype in Fig. 6, and each individual parameter is shown in Table 2. In the optimization, $\alpha = 5$ deg, $b = 152$ mm, and $t = 0.6$ mm reached their lower bound. Furthermore, $n = 1$ is obtained which is remarkable. More optimal designs can be found when these bounds are relaxed. However, these bounds are related to manufacturing limitations. Furthermore, the optimal design reached the eigenfrequency target of 20 Hz and the height constraint of 45 mm. All angles are replaced by fillets to ensure manufacturability and avoid peak stresses.

The FEA of the design can be seen in Fig. 7. The maximum stress is 0.9 MPa for a 103 μm stroke at a maximum actuation force of 1.5 N. Notice that the flexures, including the torsion-reinforcement flexures, exhibit distributed compliance, which leads to lower stress peaks.

Furthermore, in Table 3, the results of the numerical, shell, and solid models are given.

3 Experimental Validation

3.1 Test Setup. A measurement setup has been designed with the capability to accurately measure in six-DoF, achieving a resolution of 4 nm in translation and 0.3 μrad in rotation. This setup consists of an aluminum framework, a base plate, 3D-printed interfaces for all sensors, the actuator, and the CORS itself (see Fig. 8), which is positioned on rubber adjustable feet that are mounted on a TMC 3 Hz vibration isolation table with minimal amplification of resonance (8–12 dB).

3.1.1 Drive System. The CORS is actuated using a voice coil actuator (Akribis AVM40-HF-6.5) and a 3D-printed parallelogram-based linear guide connected by a thin metal wire and two eye bolts,

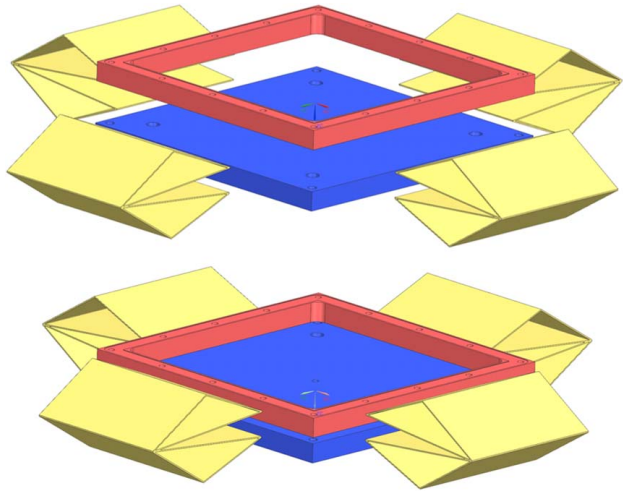

Fig. 5 CAD of CORS

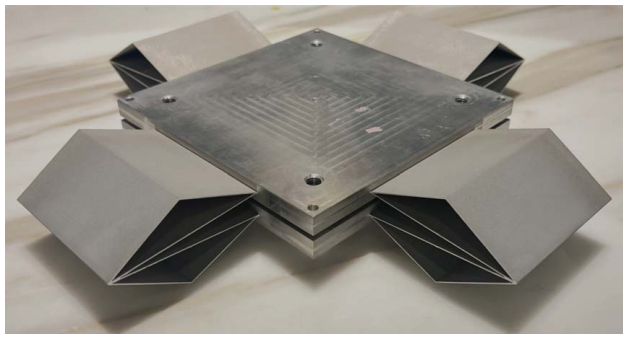

Fig. 6 Monolithic CORS, including base, flexures, and platform

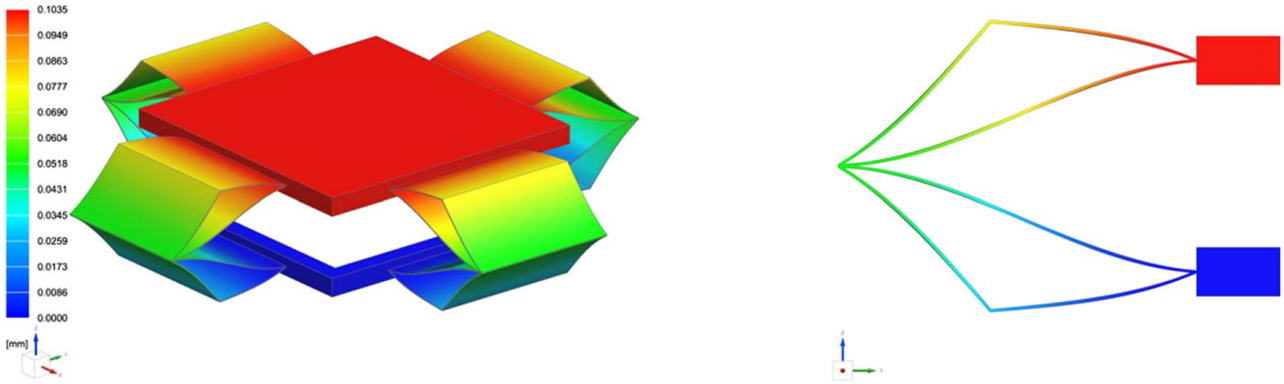

Fig. 7 Left: FEA overview CORS. Right: FEA cross section of the torsion-reinforced flexure. ***Note the distributed compliance in the six constituent flexures.***

Table 3 Simulated stiffness and error with the solid model as a reference

	Numerical	Shell model	Solid model
f_0 (Hz)	30.7	21.2	22.4
f_1 (Hz)	222.4	173.2	177.4
Error_{f_0} (%)	27%	5.6%	–
Error_{f_1} (%)	20.2%	2.3%	–
Error (x; y) (nm)	–	1.24×10^{-5}	2.52×10^{-1}

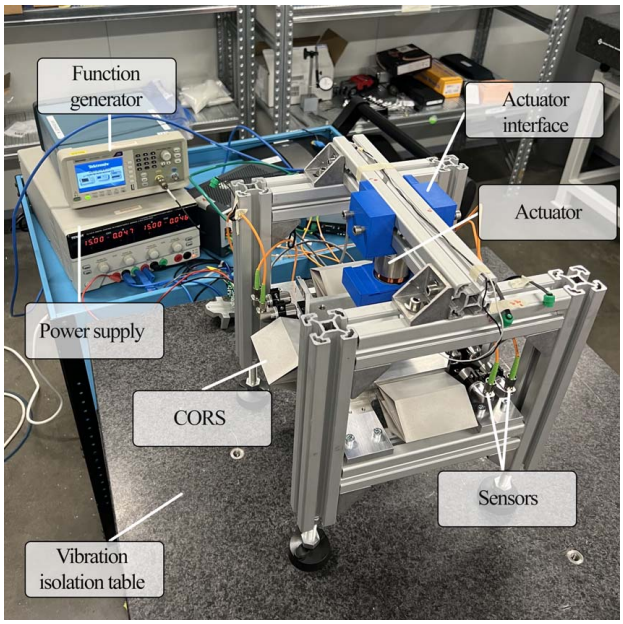

Fig. 8 Overview of the test setup

one in the center of the CORS and one in the linear guide. This is used to decouple the CORS from the actuator in all directions except the actuation direction. Voice coil actuators are direct drive actuators known for their precise linear characteristics and low hysteresis. A function generator (Tektronix AFG1062), with a maximum output current of 0.1 A, generates the input signal, while the actuator requires a maximum current of 0.29 ± 0.095 A. To generate a 6 ± 2 N force, a voltage follower is needed. This is realized using a power OPAMP (LM3886T) in a noninverting circuit combined with a voltage divider. The typical circuit, with gain 1, is simulated in PSpice beforehand.

3.1.2 Sensors. The optical sensors are based on the chromatic confocal distance measurement principle [32]. It consists of a control unit, ©*Precitec Optronik GmbH CHRocodile 2 DPS*, optical fibers, and optical probes with a 1.2 mm measuring range and an axial resolution of 4 nm. The measuring range does not allow measuring the full range of motion. Therefore, it was chosen to measure around the critical region of the range of motion. Each control unit is suitable for two probes. The prototype will be measured with four sensors; therefore, two control units are needed. The probes are perpendicularly mounted in the *XYZ*-planes, through 3D-printed interfaces, facing $\lambda/20$ rectangular mirrors mounted on the platform.

3.1.3 Test Plan and Preconditions. First, a 3D scan is made of the prototype to check the exact dimensions. This is done with the ZEISS T-SCAN hawk 2, which results in a scan that can be compared with the CAD model to gain insight into manufacturing imperfections.

The sensors and actuator have to be calibrated. The sensors are to be mounted halfway their 1.2 mm measuring range, and the required input voltage has to be found for at least 140 μm stroke.

The eigenfrequencies can be measured with the optical sensors. The CORS is triggered in the direction of motion, and a fast Fourier transform (FFT) can be obtained from an accelerometer, similar to Ref. [33], resulting in the estimated eigenfrequencies.

To measure the parasitic motions in six-DoF, the sensors are relocated once, since there were only four sensors available. First, three sensors measured the tip and tilt motions along a *Z*-stroke of 140 μm. Thereafter, the sensors were relocated and the *X* and *Y* translations were measured along a 140 μm *Z*-stroke together with the rotation around the *Z*-axis. The measured distances are transformed to translations taking the average values of two parallel sensors, and the rotations by dividing the difference between distances and the location relative to each other.

3.2 Results

3.2.1 Three-Dimensional-Scan. Visual inspection revealed no big manufacturing defects. Most of the flexure has uniform thickness along the length and width of the flexure. Visually noticeable defects are a small bump in the middle of the inner flexures and a nonconstant radius for all the fillets. The 3D-scan confirmed these findings as can be seen in Fig. 9.

3.2.2 Stiffness Measurement. The measured horizontal and vertical stiffness estimated through a FFT can be found in Fig. 10. The first eigenfrequency and its harmonics can be seen at 20.35 Hz and its multiples, respectively. Furthermore, small peaks are observed at approximately 187 Hz suggesting the second, third, and a harmonic of the first eigenfrequency.

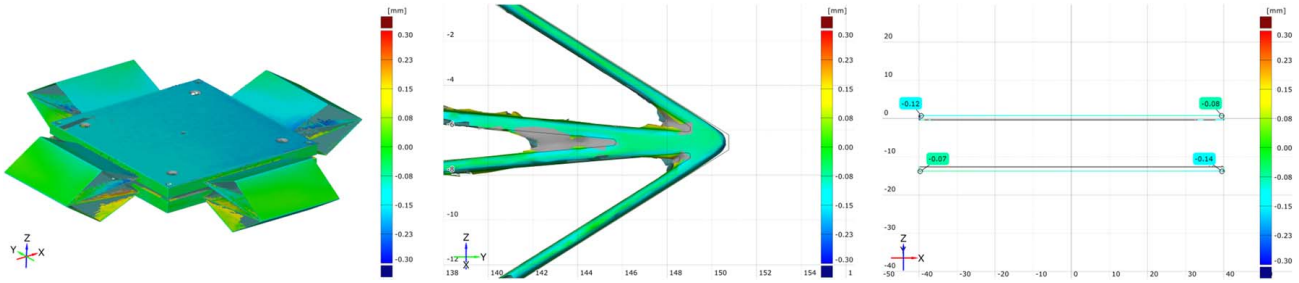

Fig. 9 3D-scan: differences between measurements and CAD-file. Left: CORS overview. Middle: fillet $R = 0.15$. Right: flexure alignment relative to the horizontal plane and each other.

3.2.3 Parasitic Motions. The parasitic motions, including noise, along the Z-stroke are plotted in Fig. 11. A linear error is shown for the parasitic X and Y translations, 0.838 nm/μm and 0.636 nm/μm, respectively. The tip (Rx) error has a range of approximately 6 μrad along the Z stroke. The tilt (Ry) error has a range of approximately 4 μrad. The measured parasitic rotation around the Z-axis is 1.44 nrad/μm stroke.

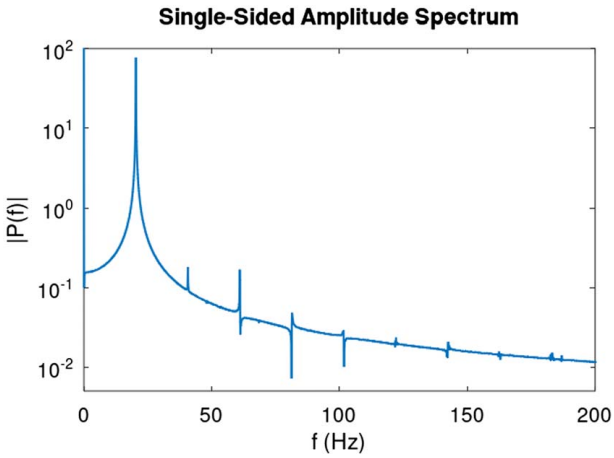

Fig. 10 Measured FFT where $f_0 = 20.35$ Hz and $f_{1,2} \approx 185$ Hz

Furthermore, a repeatability and hysteresis of approximately 10 nm and 15 nm are achieved, respectively.

4 Discussion

This design of a compact ultralinear compliant torsion-reinforced Sarrus mechanism resulted in a design that enables an open-loop motion resulting in reduced control costs and improved motion performance. Furthermore, this approach is especially beneficial in vacuum environments, where the presence of sensors and their associated cabling can significantly increase system complexity. The CORS occupies a build volume of approximately $300 \times 300 \times 45$ mm, resulting in an improved stroke-volume ratio of 0.11, compared to the ratio of Refs. [12,13] of 0.03 and 0.09, respectively. CORS has the potential to further increase this ratio, as the optimization can be adapted to a multi-objective optimization to obtain a smaller mechanism. Furthermore, a comprehensive and quantitative comparison with existing compliant mechanisms remains challenging due to the lack of standardized performance metrics and incomplete characterization in the literature. Specifically, no prior studies were found that quantify all five parasitic motions during Z-axis motion. This limits the ability to assess cross-axis coupling, dynamic stability, and true linear motion, while it can potentially mask trade-offs within the design. The presented literature does not contain a compact monolithic spatial geometry that enables a linear motion with minimized parasitic motion. A

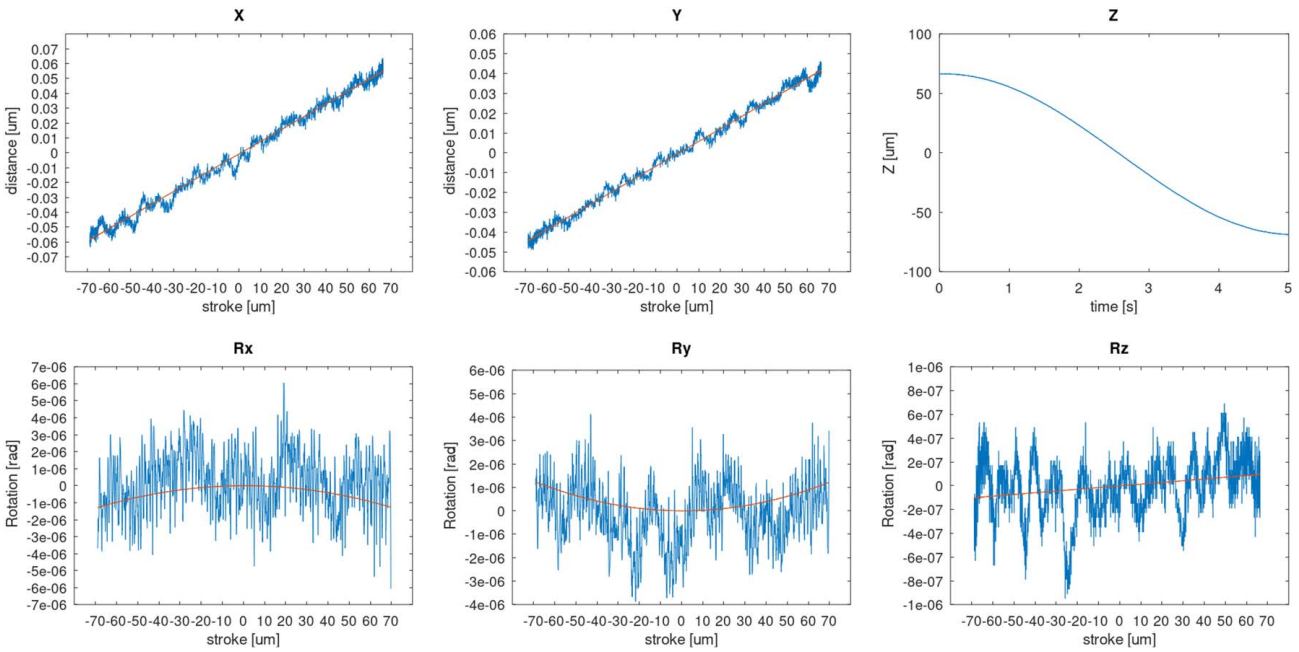

Fig. 11 Parasitic motions over 140 μm stroke at 0.1 Hz

summary of the performances within the state-of-the-art and the CORS is shown in the Appendix.

The CORS is created monolithically, which has several benefits compared to existing spatial mechanisms. The CORS has multiple overconstraints in rotation and translation around and along all axes. This could normally lead to asymmetric stresses due to potential temperature gradients, for instance. However, this effect is minimized due to its monolithic structure. Furthermore, the CORS maintains high precision repeatability, simplified assembly, predictable compliance, and more robust to thermal influences due to being monolithic.

The optimized CORS has an inter-flexure angle $2\alpha = 10$ deg, corresponding to the lower bound. This is expected since a small angle results in a higher support stiffness and low stiffness in the direction of motion. In theory, this angle could be made very small but still nonzero. If the angle is zero, it is analogous to a single leaf spring with a shortening effect during motion. However, the minimal radii of the fillets limited by the manufacturing process constrain the angles.

Furthermore, the thickness of the flexures, $t = 0.6$ mm, also reached their lower bound. Reducing the thickness will result in lowering the stiffness in the drive direction in the order of power 3, while other stiffnesses reduce linearly. The thickness could theoretically be reduced to obtain better designs. However, the wire-EDM manufacturing process used was unable to realize this. Consequently, a minimum threshold of 0.6 mm was prescribed for this parameter.

The performance of the CORS is characterized by the travel and position accuracy and the first and second eigenfrequency. The translational errors along the X and Y axes are 0.838 nm/μm and 0.636 nm/μm, respectively. However, these errors includeto change i misalignment of the mirrors relative to the direction of motion and the sensors, which will artificially affect the travel accuracy due to an Abbe error. Furthermore, the sensors have a certain drift over time due to changes in external conditions. These errors are linear; therefore, they can be filtered resulting in Fig. 12. The corrected errors along the X and Y axes are now within 10 nm for a 140 μm stroke, respectively. The measurements are limited to the resolution of the sensors, and mostly noise is observed. A fitting suggests no error along the X and Y axes, respectively.

The measured rotation around Z revealed a rotation of 1.44 nrad/μm. This results in a translational error on each platform's corner of approximately 0.8 nm/μm. The measured tip and tilt errors, Rx and Ry, have a range of approximately 6 μrad and 4 μrad over the Z stroke. These errors are not corrected for the flatness deviations of the mirrors.

The errors could be the result of the nonflatness of the mirror and the actuator misalignment. The flatness deviation of the mirror is $\lambda/20$ corresponding to 0.025 μm for visible light (≈500 nm). The deviation will cause the reflected light to be slightly distorted from its ideal position. Considering a flat mirror, we can assume that the radius of curvature is effectively infinite. Therefore, the lateral displacement is equal to the flatness deviation, 25 nm. This lateral displacement also influences the rotational measurement, which is not corrected. The error due to this nonflatness of the mirror is in the same order as the measured twist error.

FEM revealed that the actuator alignment affects the travel accuracy. If the load vector has an angle with the X and Y axes of 5.7deg relative to the Z axis, the position accuracy is 22 nm in both X and Y directions. This is also an opportunity; the measured linear error can also be calibrated physically. Figure 13 shows the translational error over a 140 μm stroke due to the angled actuator force, resulting in a normal and shear force. The measured translational X is 0.024 nm/μm. This suggests that the CORS can be calibrated even if the CORS itself does not exhibit a perfectly linear motion.

Mass on the platform has been added to investigate the effect of payload on the tip and the tilt error. It had no influence, which suggests that the CORS is stiff in Rx and Ry. However, more research is needed to obtain more precise information on the parasitic motions around the X and Y axes.

Figure 9 shows the 3D-scan of the CORS manufactured through EDM. Visual inspection revealed manufacturing errors, which are confirmed by the scan, such as nonuniform radii in the fillets of the flexure. All fillets are of different sizes and radii, for instance, the fillets seen in Fig. 9. This could lead to asymmetric flexures with different effective lengths. However, the advantage of the design is that imperfections have less influence on the motion path due to elastic averaging and that the flexures constrain motion in all directions except a Z-translation. Furthermore, a small bump in the middle of the flexures is seen as a result of the start of the EDM process. Yet, it did not affect the functionality of the CORS, so it can be concluded that errors close to the fillets and the bump in the middle are functionally acceptable. However, to avoid these errors, changes can be made in the design and manufacturing process.

The alignment of the flexures can be seen in Fig. 9. The flexures should all be perfectly aligned in the horizontal plane to avoid parasitic error. However, a deviation of at least 4 μm was measured, suggesting that the flexures are not aligned perfectly, corresponding to a misalignment of 0.5 mrad to the horizontal plane. The influence of this misalignment has been investigated using FEM. The misalignment around the Y-axis of the two opposite flexures resulted in a translational error of 69 nm in X. In practice, there is an excess of the total error budget of 5 nm. Therefore, more research has to be done into the manufacturing strategy. The alignment must be done carefully to mitigate these errors.

The FFT in Fig. 10 shows an eigenfrequency of 20.35 Hz and approximately 185 Hz. Compared to the simulation, the errors are within 10% and 5.4%, respectively. The magnitude of the parasitic

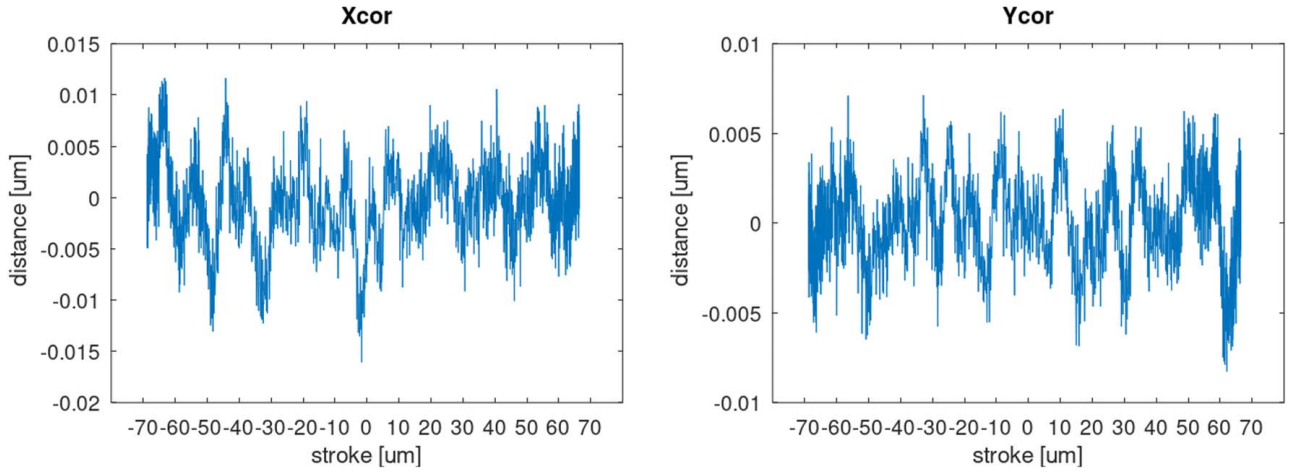

Fig. 12 Corrected parasitic *X*- and *Y*-translation

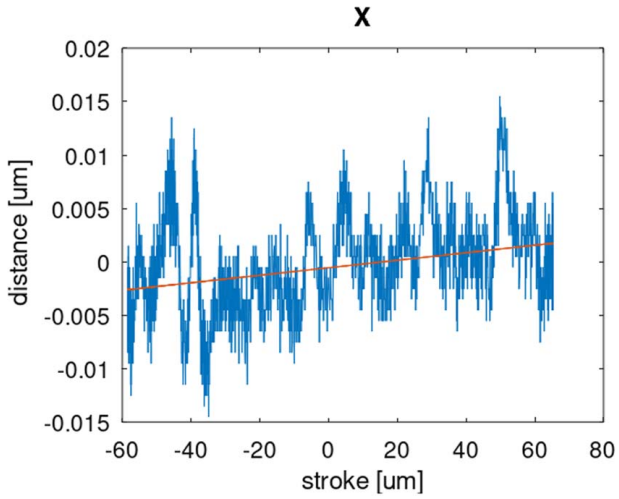

Fig. 13 Parasitic *X*-translation after *X*-calibration

eigenmode, f_1, is roughly 10^4 times smaller than that of the first eigenmode f_0. To increase the magnitude and accuracy of f_1, a different measurement method can be used, for instance, with accelerometers and a known trigger, such as an impact modal hammer. Furthermore, the difference could be explained by a deviation in mass, Young's modulus, and stiffness introduced by manufacturing imperfections. The most critical modes are the first *X* and *Y* modes and the rotational mode around *Z*, having a direct effect on the parasitic errors. These are not measured and should be investigated in the future.

The measured repeatability errors and hysteresis could be the result of friction and/or an error due to temperature drift. There are a few spots where friction can occur. First, the metal wire is stretched between two ring bolts. Tension within the wire could lead to a slip between the bolt and the wire. Furthermore, friction can occur within the actuator when the moving coil is not perfectly aligned with the permanent magnet.

To gain insight into the manufacturing tolerances, a tolerance analysis was performed. The parameter with the most influence is the thickness of the flexure. The manufacturing tolerance on the thickness is 0.02 mm. The applied tolerance gave a translational error of 11 nm. A more extensive analysis is required to obtain more information about the tolerances which can lead to a more robust design.

The fatigue life of the CORS was out of scope of this study. However, some remarks can be made. The surface roughness was considerable, which impacts the fatigue life negatively. This roughness can be reduced by repeating the EDM process multiple times. Furthermore, a postprocessing can be used to reduce the surface roughness, for instance, glass bead blasting.

In terms of measuring, changes in environmental conditions influence the accuracy of the chromatic confocal sensors. Changes in atmospheric density alter the index of refraction, affecting the wavelength of light in the sensors. This can introduce errors in distance measurements, compromising accuracy. Calibration and environmental controls can help mitigate this effect.

Furthermore, thermo-mechanical drifts refer to changes in the system behavior due to temperature fluctuations and mechanical stresses. These drifts can affect the stability and accuracy of measurements in various devices and instruments, including sensors and precision equipment. To minimize their impact, proper thermal management and mechanical stabilization techniques are often employed, such as environmental control.

5 Conclusions

This article presents the design of a compact ultralinear CORS. This architecture resulted in a smaller and easier to manufacture design compared to the existing literature. The design of the CORS represents a significant advancement in compact mechanism design, offering a compact design while maintaining critical performance metrics. A monolithic embodiment of this spatial compliant mechanism was obtained by wire-EDM in multiple directions.

The optimization process has resulted in a mechanism with small measured parasitic motions. Translation errors along the *X* and *Y* axes are 0.838 nm/μm and 0.636 nm/μm, respectively, for the critical 140 μm region of the range of motion. The rotational errors over the critical 140 μm stroke are within 6 μrad and 4 μrad around the *X* and *Y* axes, respectively. Furthermore, a small rotation occurs around the *Z* axis of 1.44 nrad/μm.

After correcting these linear trends for drift and Abbe errors, the resulting translation errors were reduced to below 10 nm (3σ) or 5 nm (1σ) in both *X* and *Y* translations. The rotational errors were down to 6 μrad (3σ) about the *X* axis, 4 μrad (3σ) about the *Y* axis, and 1.1 μrad (3σ) about the *Z* axis. These values are conservative as imperfections of the measurement mirrors are not taken into account.

The first eigenfrequency of the CORS (for its desired degree-of-freedom) is 20.35 Hz while the first parasitic eigenfrequency (for the softest constraint direction) is around 185 Hz.

Challenges such as manufacturing imperfections and misalignment were identified, highlighting the need for meticulous manufacturing processes and alignment procedures. Additionally, considerations for environmental effects on measurement accuracy, such as changes in atmospheric conditions and thermo-mechanical drifts, underscore the importance of calibration and environmental controls in ensuring reliable performance. Future research directions include further analysis of manufacturing tolerances, a more complex measurement setup, exploration of modal characteristics, and considerations for improving fatigue life through surface treatment techniques.

In general, this study provides valuable insight into the design and optimization of a compact ultralinear compliant torsion-reinforced Sarrus mechanism, with promising results for high-accuracy motion systems.

Acknowledgment

Special thanks to VDL Enabling Technologies Group Technology & Development and Delft University of Technology for providing guidance, software, resources, and manufacturing the prototype. This article was presented at the 2025 International Design Engineering Technical Conferences & Computers and Information in Engineering Conference (IDETC-CIE2025).

Conflict of Interest

There are no conflicts of interest.

Data Availability Statement

The datasets generated and supporting the findings of this article are obtainable from the corresponding author upon reasonable request.

Nomenclature

$\mathbf{d}$ = nodal displacement vector
G = shear modulus (N m^{-2})
K = stiffness (N m^{-1})
$f_{0,\ldots,n}$ = eigenfrequency (Hz)

Greek Symbols

λ = wave length (m)
σ_y = yield strength (N m^{-2})

Table 4 Performance of state-of-the-art designs and CORS

	Ref.	Flexure type: Leaf spring	Rectangular corner-filleted notch	Notch	Rotational joint	Folded leaf spring	Mechanism type: Single parallelogram	Double parallelogram	Symmetric parallelogram	Six folded leaf springs	Over constrained	Monolithic	# of flexible elements	Dimensions (mm): X	Y	Z	Stroke (mm)	Parasitic motion (nm, μ rad): ΔX	ΔY	ΔZ	$\Delta\theta_X$	$\Delta\theta_Y$	$\Delta\theta_Z$
Spatial mechanism	[12]		●	●				●			●	●	16	200	200	200	6	15	15	DoF	5	5	–
	[34]		●		●			●				●	13	140	350	450	40	180	40	DoF	9	5.3	–
	[34]		●		●		●				●		32	290	290	150	40	200	500	DoF	275	220	–
	[35] (only z-module)	●						●	●		●	●	64	250	250	121 (total of 6-DoF stage)	0.3	2232	889	DoF	≈5.1	≈5.3	≈4.4
	CORS					●		●	●		●	●	24	300	300	45	5	5 (1σ)	5(1σ)	DoF	6(3σ)	4(3σ)	1.1 (3σ)

Appendix: Summary of the Performance of State-of-the-Art Designs and CORS

See Table 4.

References

[1] Choi, B., Sreenivasan, S., Johnson, S., Colburn, M., and Wilson, C., 2001, "Design of Orientation Stages for Step and Flash Imprint Lithography," Precis. Eng., **25**(3), pp. 192–199.

[2] Lee, J., Choi, K.-B., and Kim, G.-H., 2006, "Design and Analysis of the Single-Step Nanoimprinting Lithography Equipment for Sub-100 nm Linewidth," Curr. Appl. Phys., **6**(6), pp. 1007–1011.

[3] Kim, D., Lee, D. Y., and Gweon, D. G., 2007, "A New Nano-accuracy AFM System for Minimizing Abbe Errors and the Evaluation of Its Measuring Uncertainty," Ultramicroscopy, **107**(4–5), pp. 322–328.

[4] Park, J., and Moon, W., 2005, "An XY Scanner With Minimized Coupling Motions for the High Speed AFM," Korean Society of Precision Engineering Conference, Jeju, South Korea, June 23–24, pp. 653–656.

[5] van der Maas, R., van der Maas, A., Dries, J., and de Jager, B., 2016, "Efficient Nonparametric Identification for High-Precision Motion Systems: A Practical Comparison Based on a Medical X-Ray System," Control Eng. Pract., **56**(1), pp. 75–85.

[6] Brouwer, D. M., De Jong, B., and Soemers, H., 2010, "Design and Modeling of a Six DOFs MEMS-Based Precision Manipulator," Precis. Eng., **34**(2), pp. 307–319.

[7] Gorman, J. J., Kim, Y.-S., and Dagalakis, N. G., 2006, "Control of MEMS Nanopositioners With Nano-scale Resolution," ASME 2006 International Mechanical Engineering Congress and Exposition, Chicago, IL, Nov. 5–10, Vol. 47756, pp. 151–159.

[8] Van Schoot, J., 2023, "The Moore's Law Machine: The Next Trick to Tinier Transistors Is High-Numerical-Aperture EUV Lithography," IEEE Spectrum, **60**(9), pp. 44–48.

[9] Smith, S. T., 2003, *Foundations of Ultra-precision Mechanism Design*, CRC Press, London.

[10] Gallego, J. A., and Herder, J., 2009, "Synthesis Methods in Compliant Mechanisms: An Overview," ASME 2009 International Design Engineering Technical Conferences and Computers and Information in Engineering Conference, San Diego, CA, Aug. 30–Sept. 2, Vol. 49040, pp. 193–214.

[11] Radaelli, G., and Herder, J., 2016, "A Monolithic Compliant Large-Range Gravity Balancer," Mech. Mach. Theory, **102**(1), pp. 55–67.

[12] Koster, M. P., 1994, "Constructies voor het nauwkeurig bewegen en positioneren," Mikroniek, **34**(2), pp. 38–42.

[13] Cosandier, F., 2013, *Conception d'axes motorisés rectilignes d'ultra-haute précision*, EPFL.

[14] Duarte, R., Howells, M. R., Hussain, Z., Lauritzen, T., and McGill, R., 1997, "A Linear Motion Machine for Soft X-Ray Interferometry," Lawrence Berkeley National Lab. (LBNL), Berkeley, CA.

[15] Smith, S., Chetwynd, D., and Bowen, D., 1987, "Design and Assessment of Monolithic High Precision Translation Mechanisms," J. Phys. E: Sci. Instrum., **20**(8), p. 977.

[16] Pousset, N., Salgado, J., and Vailleau, G.-P., 2009, "Étalonnage de micromètres objets par microscopie optique," REVUE FRANÇAISE DE MÉTROLOGIE n18, **2009-2**.

[17] Becker, P., Seyfried, P., and Siegert, H., 1987, "Translation Stage for a Scanning X-Ray Optical Interferometer," Rev. Sci. Instrum., **58**(2), pp. 207–211.

[18] Jones, R., 1951, "Parallel and Rectilinear Spring Movements," J. Sci. Instrum., **28**(2), p. 38.

[19] Alemanni, M., Mana, G., Pedrotti, G., Strona, P., and Zosi, G., 1986, "On the Construction of a Zerodur Translation Device for X-Ray Interferometric Scanning," Metrologia, **22**(1), p. 55.

[20] Tissot-Daguette, L. B., Schneegans, H. P.-M. B., Gubler, Q., Baur, C., and Henein, S., 2022, "Rectilinear Translation Four-Bar Flexure Mechanism Based on Four Remote Center Compliance Pivots," Proceedings of the 22nd International Conference of the European Society for Precision Engineering and Nanotechnology, euspen, Paper No. CONF.

[21] Parise, John J., Howell, Larry L., and Magleby, Spencer P., 2001, "Ortho-Planar Linear-Motion Springs," Mech. Mach. Theory, **36**(11–12), pp. 1281–1299.

[22] Chen, S.-C., Golda, D., Herrmann, A., and Slocum, A. H., 2004, "Design of an Ultra Precision Diaphragm Flexure Stage for Out-of-Plane Motion Guidance," ASME 2004 International Design Engineering Technical Conferences and Computers and Information in Engineering Conference, Salt Lake City, UT, Sept. 28–Oct. 2, Vol. 46954, pp. 1015–1021.

[23] Sarrut, P.F., 2012, "Note sur la transformation des mouvements rectilignes alternatifs, en mouvements circulaires; et réciproquement," Comptes Rendus Hebdomadaires des Séances de l'Académie des Sciences, **36**, pp. 1036–1038.

[24] Soemers, H., 2010, "Design Principles for Precision Mechanisms," T-Point Print.

[25] Rommers, J., Naves, M., Brouwer, D., and Herder, J. L., 2022, "A Flexure-Based Linear Guide With Torsion Reinforcement Structures," ASME J. Mech. Rob., **14**(3), p. 031013.

[26] Meinders, N., 2021, "Compensating Parasitic Motions and Cross-Couplings in Compliant Mechanisms: The Development of a New Compensation Strategy to Diminish Unwanted Motions," Master Thesis, TU Delft.

[27] Brouwer, D. M., Folkersma, G. K. G. P., Boer, S. E., and Aarts, R. G. K. M., 2013, "Exact Constraint Design of a Two-Degree of Freedom Flexure-Based Mechanism," ASME J. Mech. Rob., **5**(4), p. 041011.
[28] de Jong, J. J., Nijenhuis, M., and Brouwer, D. M., 2022, "A Massively Overconstrained and Statically Balanced Flexure Mechanism for a 20 kN Load Capacity," 37th Annual Meeting of the American Society for Precision Engineering, ASPE 2022, Bellevue, WA, Oct. 10–14, pp. 98–101.
[29] Awtar, S., Shimotsu, K., and Sen, S., 2010, "Elastic Averaging in Flexure Mechanisms: A Three-Beam Parallelogram Flexure Case Study," ASME J. Mech. Rob., **2**(4), p. 041006.
[30] Dwarshuis, K., De Jong, J., and Brouwer, D., 2025, "Design of an Underactuated, Flexure-Based Gripper, Actuated Through a Push–Pull Flexure," ASME J. Mech. Rob., **17**(6), p. 061009.
[31] Siemens, 2008, "SHERPA—An Efficient and Robust Optimization/Search Algorithm," Red Cedar Technology, Tech. Rep. WP-1023.
[32] Ruprecht, A. K., Pruss, C., Tiziani, H. J., Osten, W., Lucke, P., Last, A., Mohr, J., and Lehmann, P., 2005, "Confocal Micro-Optical Distance Sensor: Principle and Design," CLEO/Europe - EQEC 2005 – 17th International conference on photonics in Europe, Munich, Germany, June 12–17, pp. 128–135.
[33] Pham, M. T., Yeo, S. H., Teo, T. J., Wang, P., and Nai, M. L. S., 2019, "Design and Optimization of a Three Degrees-of-Freedom Spatial Motion Compliant Parallel Mechanism With Fully Decoupled Motion Characteristics," ASME J. Mech. Rob., **11**(5), p. 051010.
[34] Cosandier, F., Eichenberger, A., Baumann, H., Jeckelmann, B., Bonny, M., Chatagny, V., and Clavel, R., 2014, "Development and Integration of High Straightness Flexure Guiding Mechanisms Dedicated to the METAS Watt Balance Mark II," Metrologia, **51**(2), p. S88.
[35] Zhang, Q., Dong, H., Zhang, Z., Cai, X., Gao, Y., and Dong, W., 2025, "A Kinematically Decoupled 6-Degree-of-Freedom Nanopositioning Stage With Minimized Crosstalk Based on Flexure Hinges," ASME J. Mech. Rob., **17**(11), p. 111010.